

Decorrelating Ambiguities in SAR Interferometry through Slight PRI Variation

Michelangelo Villano, *Senior Member, IEEE*, Maxwell Nogueira Peixoto, Nertjana Ustalli, *Member, IEEE*, Josef Mittermayer, Gerhard Krieger, *Fellow, IEEE*, and Alberto Moreira, *Fellow, IEEE*

Abstract—Synthetic aperture radar (SAR) interferometry is a well-established technique for producing high-resolution digital elevation models (DEMs) of the Earth’s surface and measuring displacements on different time scales. Observations of SAR interferograms, however, show that azimuth ambiguities can be coherently imaged and may lead to phase biases and coherence losses that significantly degrade the interferometric performance. Whereas imposing very low ambiguity levels may represent a severe design constraint for a spaceborne SAR system, a slight variation of the pulse repetition interval (PRI) is a new, simple, yet effective technique to decorrelate ambiguities, which in turn reduces the phase biases and coherence losses without substantially affecting the imaged swath width. An additional benefit of the PRI variation is that range ambiguities also become decorrelated. This paper addresses two cases: For the repeat-pass case, slightly different pulse repetition frequencies (PRFs) can be used for the two acquisitions and the minimum required PRF difference can be analytically derived resorting to the power spectral density of the ambiguous signals; For the single-pass case, a slight variation of the PRI during the common acquisition is an effective solution, in case an along-track baseline is present. In particular, a square wave PRI variation scheme outperforms sinusoidal or random ones. Finally, simulations using TanDEM-X data are presented to show the improvement in interferogram and DEM quality resulting from ambiguity decorrelation. This work is relevant for the design of future spaceborne interferometric SAR systems and for the enhanced exploitation of current ones.

Index Terms—Azimuth ambiguities, interferometry, microwave remote sensing, synthetic aperture radar (SAR).

I. INTRODUCTION

SYNTHETIC aperture radar (SAR) interferometry exploits the coherent combination of two or more SAR images for a large number of applications. If two images, often referred to as the master and slave images, are acquired from slightly different viewing angles, a digital elevation model (DEM) of the observed scene can be formed, while images acquired at different times from the same position allow for measurements of, e.g., ocean current velocity using along-track SAR interferometry or radial displacements using differential interferometry [1]–[4]. The accuracy of the resulting products ultimately depends on the complex correlation (or coherence)

between the two SAR images, which is the product of the contributions of various decorrelation sources, such as thermal noise, quantization noise, baseline decorrelation, volume decorrelation, Doppler decorrelation, temporal decorrelation, co-registration and processing errors, as well as range and azimuth ambiguities [5]–[6].

Azimuth ambiguities were initially accounted for through a decorrelation contribution $\gamma_{amb,az}$ given by

$$\gamma_{amb,az} = 1/(1 + AASR) \quad (1)$$

where $AASR$ is the azimuth ambiguity-to-signal ratio (AASR), i.e., similarly to thermal noise [7]–[8]. Observations of several TanDEM-X interferograms, such as the one in Fig. 1 acquired over the Franz Josef Land, Russia, however, have shown that azimuth ambiguities may be coherently imaged and lead to significant interferometric phase biases φ_{bias} and modulations of the coherence magnitude γ , which can be analytically described by the following expressions, derived in [9]:

$$\varphi_{bias} = \arg \left\{ 1 + AASR_{local} \frac{\gamma_a}{\gamma_m} e^{j(\varphi_{0,a} - \varphi_{0,m})} \right\} \quad (2)$$

$$\gamma = \frac{1}{1 + AASR_{local}} \cdot \sqrt{\gamma_m^2 + AASR_{local}^2 \gamma_a^2 + 2 AASR_{local} \frac{\gamma_a}{\gamma_m} \cos(\varphi_{0,a} - \varphi_{0,m})} \quad (3)$$

where $AASR_{local}$ is the local azimuth ambiguity-to-signal ratio, γ_m and $\varphi_{0,m}$ are the coherence magnitude and interferometric phase of the ambiguity-free interferogram, respectively, and γ_a and $\varphi_{0,a}$ are the coherence magnitude and interferometric phase of the interferogram of the ambiguities, respectively.

A spectral-based technique to estimate the local azimuth ambiguity-to-signal ratio is presented in [10], where it is also shown that the latter ratio is likely to be larger than -10 dB in low-backscatter areas and can even reach 0 dB in some cases. As discussed in [11], a local AASR of -5 dB results in a phase bias characterized by a standard deviation of 5 to 10 degrees (depending on the signal-to-noise ratio) and a decorrelation

Manuscript received Month XX, 202X; revised Month XX, 202X; accepted Month XX, 202X. Date of publication Month XX, 202X; date of current version Month XX, 202X.

M. Villano, M. Nogueira Peixoto, N. Ustalli, J. Mittermayer, G. Krieger, and A. Moreira are with the German Aerospace Center (DLR), Microwaves and

Radar Institute Oberpfaffenhofen, 82234 Wessling, Germany (e-mail: michelangelo.villano@dlr.de).

Color versions of one or more of the figures in this paper are available online at <http://ieeexplore.ieee.org>.

Digital Object Identifier XX.XXXX/TGRS.202X.XXXXXXX.

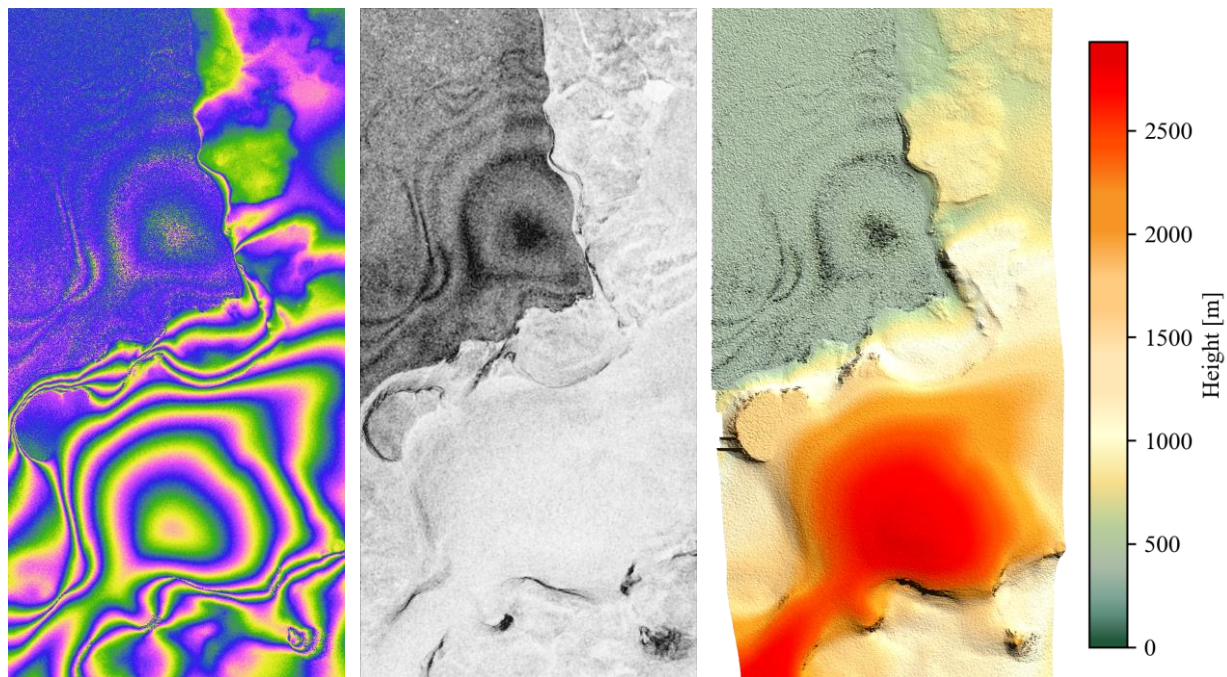


Fig. 1. Interferometric phase (left), magnitude of the complex coherence (center) and DEM (right) of a detail of a TanDEM-X interferogram affected by azimuth ambiguities, acquired over the Franz Josef Land, Russia. The horizontal and vertical axes represent ground range (5.12 km) and azimuth (10.24 km), respectively. The azimuth ambiguities of the mountain in the lower part of the image are seen in the upper part as a bias in the sea ice region.

contribution due to azimuth ambiguities in the order of 0.7-0.8. The aforementioned decorrelation and phase bias contributions are critical to be accounted for in the overall height error and coherence budget. One could reduce the local AASR by imposing a lower AASR requirement in the overall design, but this would drive the complexity and the cost of the SAR system, e.g., by increasing the length of the azimuth antenna and introducing a weighting in the azimuth antenna to decrease the sidelobes. Please note that a simple increase of the PRF leads to a decrease of the swath width in order to keep the range ambiguities at an acceptable level.

The local ambiguity-to-signal ratio could also be reduced by removing azimuth ambiguities through a postprocessing step [12]-[19]. A Wiener filter could be applied, as proposed in [13], but this would result in a resolution degradation, which turns into a reduction of the number of interferometric looks and thus of the coherence. Ambiguities could also be coherently subtracted directly from the interferogram, as was first demonstrated in 2011 in a DLR-internal study to reduce the phase errors and coherence losses in the TanDEM-X interferogram of Fig. 1 (see also [9], [11]). This technique was then further elaborated for short-baseline along-track interferometry in [20] and [21], but the accurate and fully autonomous estimation of the complex scaling coefficient makes this technique challenging.

Equations (2) and (3) suggest that the phase bias and the coherence loss can also be controlled by limiting the coherence magnitude of the interferogram of the ambiguities γ_a , i.e., by decorrelating the azimuth ambiguities of the master and slave images. If total decorrelation is achieved, there is no interferometric phase bias anymore and the decorrelation

contribution degenerates into the expression in (1), where AASR has still to be understood as the local one, i.e., the decorrelation contribution due to azimuth ambiguities is similar to the one due to thermal noise.

γ_a is influenced by the acquisition geometry, which in some cases makes the azimuth ambiguities of the master and slave images be mutually shifted and therefore decorrelated. Under the conservative assumption that the acquisition geometry leads to full overlap of the ambiguities, ambiguity decorrelation can still be achieved by acting on the mutual sampling of the master and slave images.

The paper is organized as follows. Section II addresses the repeat-pass case, for which an analytical expression of the minimum required pulse repetition frequency (PRF) difference between the two acquisitions is derived. Section III considers instead the single-pass case and presents different pulse repetition interval (PRI) variation schemes together with the resulting swath width reduction and ambiguity decorrelation. In Section IV the impact of ambiguity decorrelation on interferogram and DEM quality is assessed through simulations using TanDEM-X data. Conclusions are drawn in Section V.

II. REPEAT-PASS SAR INTERFEROMETRY

If the master and slave images are acquired at different times, the adoption of slightly different PRFs in the two acquisitions might suffice to decorrelate azimuth ambiguities. This case also includes the pursuit monostatic mode of TanDEM-X [6], where the time lag between the two acquisitions is in the order of a few seconds.

The minimum PRF difference ΔPRF required for decorrelation can be obtained by imposing that the relative

azimuth shift Δx of the first-order azimuth ambiguities between the two acquisitions is larger than the autocorrelation length ℓ_a of the ambiguous signals times the satellite speed.

The azimuth shift Δx is given by [22]-[24]

$$\Delta x = \frac{\lambda R_0 \Delta PRF}{2 v_S} \quad (4)$$

where λ is the wavelength, R_0 is the radar-target range of closest approach, and v_S is the satellite speed, whereas the autocorrelation length ℓ_a of the ambiguous signals depends on the power spectral density (PSD) of the ambiguous signals, therefore on both the azimuth antenna pattern and the selected PRF. Fig. 2 shows the PSDs of the main signal and the first-order left ambiguity for TanDEM-X, which is characterized by a rectangular antenna with length $L = 4.8$ m and $\lambda = 0.03$ m, with $PRF = 3000$ Hz. It also provides the corresponding normalized autocorrelation functions, obtained as inverse Fourier transforms of the PSDs. Although strictly speaking the PSD and the autocorrelation function are different for the two ambiguous signals due to the different PRFs, a difference in the order of few Hz can be neglected. As is apparent, due to the shape of the PSD of the ambiguous signals, the autocorrelation length of the ambiguous signals can be several times (i.e., in this example about five times) larger than that of the main signal, which is approximately equal to $L/(2 v_S)$, i.e., 0.3 ms. The autocorrelation length becomes smaller for higher PRFs, i.e., around 5000 Hz, which are, however, unlikely to be used within typical TanDEM-X acquisitions.

Defining as α the ratio of the autocorrelation lengths of the ambiguous and main signals, it holds

$$\Delta PRF > \alpha \frac{L v_S}{\lambda R_0} \quad (5)$$

where conservative values of α of at least 5 should be assumed. In other words, due to the shape of the PSD of the ambiguous signals, the minimum required PRF difference is such that it mutually shifts the first-order azimuth ambiguities by five azimuth resolution cells. For higher-order azimuth ambiguities, the azimuth shift will be larger by a factor k equal to the order of the ambiguity, while the autocorrelation length of the ambiguous signal will be in the worst case and for a rectangular antenna in the same order of magnitude as the one obtained for first-order ambiguities.

For TanDEM-X, a $\Delta PRF \cong 8$ Hz is required for a $PRF \cong 3000$ Hz, which does not significantly influence the width of the common swath to be imaged. As is apparent from its derivation, this simple model does not account for the defocusing of azimuth ambiguities resulting from the wrongly compensated range cell migration. However, two-dimensional (2-D) simulations show that (5) still provides a good estimate of the ΔPRF value required for ambiguity decorrelation. The simulations are carried out by convolving the 2-D impulse responses of the system with complex white Gaussian signals representing distributed targets (fully developed speckle) and

then estimating the coherence of the first-order azimuth ambiguities of the master and slave images as a function of the PRF difference ΔPRF . Fig. 3 shows the coherence of the first-order azimuth ambiguities as a function of ΔPRF obtained from 2-D simulations for TanDEM-X with a $PRF = 3000$ Hz (the coherence reduces significantly at $\Delta PRF \cong 8$ Hz, as expected), for a high-resolution X-band system with a 2.4-m-long antenna and a chirp bandwidth $B_r = 600$ MHz, and for an L-band system with a 10-m-long antenna. In all cases there is full agreement with the estimates obtained using (5).

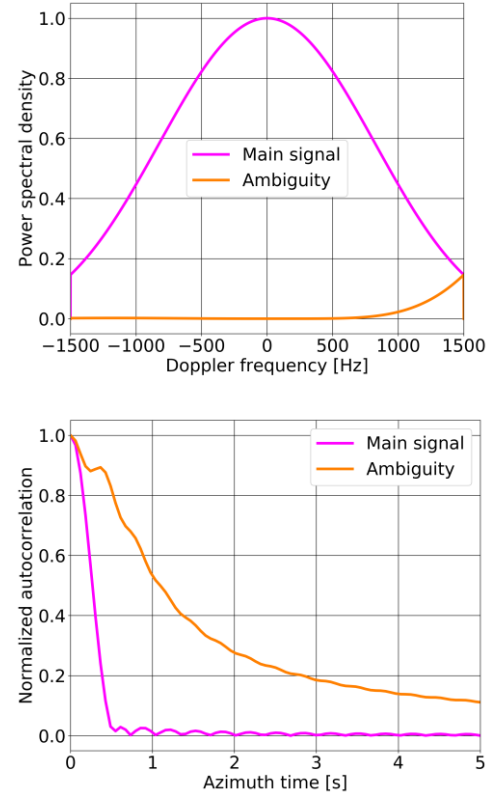


Fig. 2. Power spectral densities normalized to maximum of the main signal (top) and normalized autocorrelation functions (bottom) of the main signal and the first-order left ambiguity for TanDEM-X with $PRF = 3000$ Hz.

Note that for the TanDEM-X case, the minimum value of ΔPRF obtained using (5) is smaller than the PRF difference $\Delta PRF_{no\ overlap}$ required to avoid overlapping of the first-order azimuth ambiguities of the master and slave images, which is a sufficient condition for ambiguity decorrelation. $\Delta PRF_{no\ overlap}$ can be obtained by imposing that the azimuth shift Δx is larger than the azimuth extension of the first-order azimuth ambiguities (in meters) E_a , which, accounting for the defocusing due to the wrongly compensated range-cell migration, is given by [22]-[24]

$$E_a \cong \frac{PRF \lambda^2 R_0}{4 v_S \delta_r} \quad (6)$$

where δ_r is the range resolution of the system. It holds

$$\Delta PRF_{no\ overlap} > \frac{\lambda PRF}{2 \delta_r} \quad (7)$$

For a TanDEM-X acquisition with $B_r = 100$ MHz, a PRF difference in the order of $\Delta PRF_{no\ overlap} \cong 30$ Hz for $PRF \cong 3000$ Hz is required to avoid overlap of the first-order azimuth ambiguities, i.e., larger than the PRF difference required for ambiguity decorrelation. This means that azimuth ambiguities can be decorrelated, even if they partially overlap.

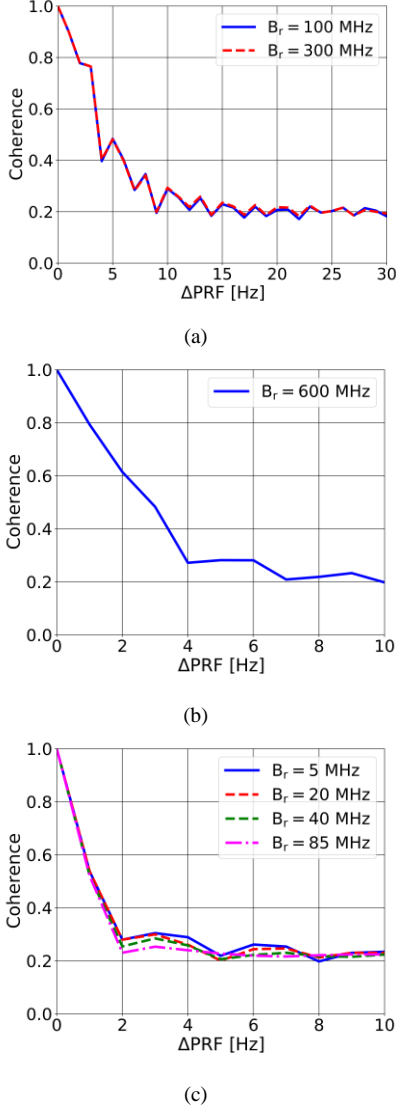


Fig. 3. Coherence of the ambiguities for repeat-pass SAR interferometry as a function of the PRF difference between the two acquisitions ΔPRF for (a) TanDEM-X with a $PRF = 3000$ Hz, (b) a high-resolution X-band system with a 2.4-m-long antenna, (c) a L-band system with a 10-m-long antenna, and different values of the chirp bandwidth B_r .

Furthermore, as a consequence of the use of different PRFs, range ambiguities of the master and slave images will also be relatively displaced in range and will not overlap nor produce any coherent interference, as long as

$$\left| \frac{1}{PRF + \Delta PRF} - \frac{1}{PRF} \right| \frac{c_0}{2} \cong \frac{\Delta PRF}{PRF^2} \frac{c_0}{2} > \delta_r \quad (8)$$

where c_0 is the speed of light and where it has been assumed that the first-order range ambiguity is only smeared in azimuth (due to the mismatch in the azimuth compression) and not in range [22]. For the TanDEM-X example, where the minimum required PRF difference to achieve ambiguity decorrelation was calculated to be $\Delta PRF \cong 8$ Hz for a $PRF = 3000$ Hz, (8) is already verified for slant range resolutions better than 133.2 m, i.e., the slight PRF difference has the additional benefit of mutually shifting range ambiguities of the master and slave images and preventing any coherent interference of range ambiguities.

If a large interferometric stack has to be created, the selection of numerous distinct PRFs, which lead to mutually decorrelated ambiguities, is constrained by the timing (or diamond) diagram. Those constraints can be relaxed adopting techniques based on waveform variation and dual-focus postprocessing that help the system designer get rid of the nadir interference [25], [26]. For example, in the presence of the sole transmit interference, for TanDEM-X and a ground swath width of 30 km, a PRF span ranging from about 50 Hz (far range) to about 100 Hz (near range) is available around $PRF = 3200$ Hz. This means that, assuming a total decorrelation for $\Delta PRF \cong 8$ Hz, a number of distinct PRFs ranging from 7 (far range) to 13 (near range) can be used. If a larger number of distinct PRFs is needed, a significant ambiguity decorrelation is still obtained for smaller PRF spacing, e.g., the coherence drops to around 0.4 for $\Delta PRF \cong 4$ Hz in the TanDEM-X example of Fig. 3 (a). Moreover, the residual phase biases of different interferograms within the stack will be randomly distributed with a mean interferometric phase equal to zero, therefore the resulting phase bias for an image stack will depend on the overall processing and is likely to become successively smaller, as more and more data sets are combined.

III. SINGLE-PASS SAR INTERFEROMETRY

If the master and slave images are acquired at the same time and a single transmitter is used, the adoption of a slight PRI variation during the acquisition could help decorrelate ambiguities, as long as a non-zero along-track baseline B_a is present. The impulse response function (IRF) in proximity of the ambiguities, in fact, is azimuth-variant in case of variable PRI and the along-track baseline induces (after co-registration) a relative azimuth time shift δ_u between the available azimuth samples of the master and slave images roughly given by

$$\delta_u \cong \frac{B_a}{2v_g} \quad (9)$$

where v_g is the ground velocity and where a bistatic configuration has been assumed with the same satellite transmitting all pulses (Fig. 4).

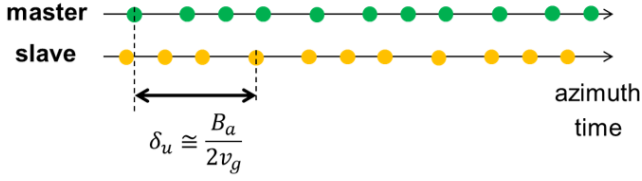


Fig. 4. Relative azimuth time shift of the samples after co-registration resulting from a non-zero along-track baseline.

Under the assumption that the acquisition geometry leads to overlap of the ambiguities, the absence of an along-track baseline leads to the same IRFs for the master and slave image independently of the PRI variation scheme. At the same time, the presence of an along-track baseline without a PRI variation is not sufficient to avoid correlation of the ambiguities, as the ambiguities of the master and slave images might be characterized by different phases, but their phase difference would still be constant (the latter is also the case in Fig. 1).

In presence of the aforementioned relative shift, the raw data of master and slave could be resampled, e.g., using best linear unbiased (BLU) interpolation [27]-[30], to a uniform grid before focusing and interferogram formation. The coefficients of the BLU interpolation depend on the spectrum of the main signal and are not the optimal ones to resample the ambiguous signal, which has a different spectrum and will therefore be resampled in a wrong way and, in general, in a different way in the master and slave images, leading to a decorrelation of the ambiguities.

An additional advantage of a PRI variation, especially if followed by a “wrong” resampling, is that ambiguities will be further smeared compared to the constant PRF case and will be therefore characterized by a reduced range resolution. This corresponds to a smaller critical baseline for the ambiguities, which could in turn result in a decorrelation of the ambiguities of distributed scatterers.

A. PRI Variation Schemes

The PRI variation scheme will influence the positions of the blind ranges for each range line. In particular, the positions of the blind ranges depend on the moving sum of a number of consecutive PRIs equal to the number of traveling pulses n_t [32], which is roughly given by

$$n_t \cong \frac{2R_0}{c_0 PRI_{mean}} \quad (10)$$

where c_0 is the speed of light and PRI_{mean} is the mean PRI.

The continuous variation of the PRI recalls staggered SAR systems, which include BLU interpolation as an integrating part of the concept [27]-[30], are characterized by smeared and decorrelated range and azimuth ambiguities [24], [32], and are well suited for interferometry [33]-[35]. While in staggered SAR, however, a PRI variation is required that ideally shifts blind ranges to all possible positions across the swath in order to have them uniformly distributed, for the scope of this work the PRI variation should allow keeping the width of the imaged

swath. Considering that for most SAR systems the imaged swath is smaller than the maximum one allowed by the timing (or diamond) diagram due to, e.g., signal-to-noise ratio or ambiguity requirements, a small variation of the blind ranges across the synthetic aperture can be tolerated.

Three PRI variation schemes are considered in the following, namely:

- **Sinusoidal PRI Variation**, whose PRIs can be written as

$$PRI_k = PRI_{mean} \left(1 + A \sin \frac{2\pi k}{N} \right), \quad k = 0, \dots, N-1 \quad (11)$$

where A is the amplitude of the PRI variation, e.g., $A = 0.01$ means that the PRI variation is $\pm 1\%$ with respect to PRI_{mean} , and N is the length (to be understood as number of PRIs) of the sequence, which repeats then periodically;

- **Square Wave PRI Variation**, whose PRIs can be written as

$$PRI_k = \begin{cases} PRI_{mean}(1+A), & k = 0, \dots, N/2-1 \\ PRI_{mean}(1-A), & k = N/2, \dots, N-1 \end{cases} \quad (12)$$

with N even to keep the symmetry. In this case only two distinct PRIs are used, a first PRI, $PRI_{mean}(1+A)$, is repeated $N/2$ times, then a second PRI, $PRI_{mean}(1-A)$, is repeated $N/2$ times, then the first PRI is repeated again $N/2$ times and so on.

- **Random PRI Variation** (to be intended as a sequence of N random PRIs, which repeat periodically), whose PRIs can be written as

$$PRI_k = PRI_{mean}[1 + A a_k], \quad k = 0, \dots, N-1 \quad (13)$$

where a_k is an independent realization of a random variable with uniform distribution in the interval $[-1; 1]$. The advantage of repeating the same sequence of random realizations is justified in Section III.B.

Note that the three PRI variation schemes are expressed so that they are characterized by the same PRI span, if the value of A is the same. Fig. 5 shows the PRI trend for two cycles of PRI variation for the three presented sequences with $PRI_{mean} = 0.303$ ms, $N = 100$ and $A = 0.007$.

B. Swath Reduction

If the length N of the sequence of PRIs is much larger than the number of traveling pulses n_t , the maximum achievable swath width W_S for a sinusoidal or a square wave PRI variation is approximately given by

$$W_S \cong (1 - 2A n_t) W_{S_{const}} \quad (14)$$

where $W_{S_{const}}$ is the maximum swath width obtained for a constant PRI equal to PRI_{mean} , e.g., for $n_t = 16$ and $A = 0.001$, the maximum swath width would reduce by 3.2%; hence the need of keeping the amplitude A very small. The formula is derived under the conservative assumption that the n_t PRIs adjacent to the maximum PRI are all equal to the maximum

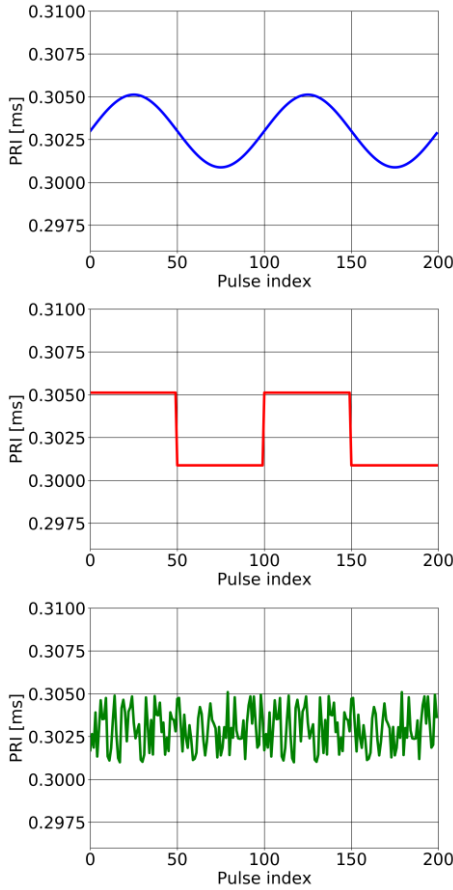


Fig. 5. Sinusoidal (top), square wave (center), and random (bottom) PRI variation schemes provided in (11), (12), and (13), respectively, for $PRI_{mean} = 0.303$ ms, $N = 100$ and $A = 0.007$. Two cycles are displayed.

PRI.

Still under the assumption that the length N of the PRI sequence of PRIs is much larger than the number of traveling pulses n_t , the assessment of the swath reduction for the periodic random PRI variation of (13) cannot be approximated in a straightforward way as in the case of sinusoidal and square wave PRI variations, but requires some further considerations. Due to the randomness of the PRI, theoretically the swath reduction could also reach the value provided in (14), but this worst case would only happen in the very unlikely case that n_t consecutive independent realizations of a_k are all equal or almost equal to 1 (or -1). A more reasonable approach is to resort to probability theory. The sum of n_t PRIs characterized as in (13), i.e., uniformly distributed, follows the Irwin-Hall distribution, which for large values of n_t can be approximated by a Gaussian distribution, whose standard deviation (relative to PRI_{mean}) σ is given by $A\sqrt{n_t}/\sqrt{3}$. By considering an interval of $\pm 2\sigma$ (95% rule) and approximating, we obtain the following expression for the maximum achievable swath width W_S , which looks, but for a square root, very similar to (14):

$$W_S \cong \left(1 - \frac{4}{\sqrt{3}} A\sqrt{n_t}\right) W_{S_{const}} \approx (1 - 2 A\sqrt{n_t}) W_{S_{const}} \quad (15)$$

The comparison of (15) to (14) highlights that for a random PRI variation the same swath reduction is obtained for a much larger PRI span (i.e., four times larger for $n_t = 16$) compared to the sinusoidal and square wave cases. While for sinusoidal and square wave PRI variations, in fact, the swath reduction is proportional to the number of traveling pulses n_t , for periodic random PRI variation the swath reduction is approximately proportional to the square root of the number of traveling pulses. This is shown with an example in Fig. 6, which refers to a TanDEM-X like system characterized by a pulse width of 25 μ s and a mean pulse repetition interval $PRI_{mean} = 0.303$ ms, corresponding to a mean PRF of 3300 Hz. For the sinusoidal and square wave PRI variations the parameters $N = 100$ and $A = 0.007$ have been used (resulting according to (14) to an approximate swath reduction of about 22.4%), while for the periodic random PRI variation the parameters $N = 100$ and $A = 0.007\sqrt{n_t} = 0.028$ have been used, which results in the same swath reduction (less than 14 km in ground range). Note that the areas in blue/red/green include not only the blind ranges in the raw data, but also areas characterized by reduced range resolution after pulse compression [28]-[29].

A larger PRI span implies a further smearing of azimuth ambiguities, which might help reducing the critical baseline, as discussed above. The interval has been chosen around $\pm 2\sigma$ and not larger, because the length of the PRI sequence is limited and so is the number of realizations. This justifies repeating the same random sequence rather than having a very long one (requirements on the minimum sequence length will be discussed in Section III.C). An “unfortunate” realization, in fact, can just be discarded, as the system designer can choose the PRI variation to be adopted for the acquisition in advance.

If the length of the PRI sequence N is instead equal to the number of traveling pulses n_t (or to $n_t - 1$), larger PRI span (and namely amplitudes A) can be exploited without incurring in a significant swath reduction. For all three considered PRI variations, in fact, the moving sum will be constant for one of the two blind ranges delimiting the swath, due to the fact that the addends of the moving sum stay the same, and almost constant for the other one, where the moving sum includes $N - 1$ out of the N values. In this case for all three considered PRI variations the same PRI span leads to the same swath reduction and the maximum achievable swath width W_S can be approximated as

$$W_S \cong (1 - A)W_{S_{const}} \quad (16)$$

In this case, in fact, the maximum relative variation of the blind range is $2A$ (i.e., the highest possible difference between 2 PRIs of the sequence), but the swath reduction is only due to one of the two blind ranges.

Fig. 7 shows an example of the case $N = n_t$ for the three considered PRI variations. It is apparent that the swath reduction is much smaller than in Fig. 6, although the PRI span is much larger ($A = 0.05$ vs. $A = 0.007$). For $N = n_t - 1$, the moving sum is constant for the closer of the two blind ranges

and (16) still holds.

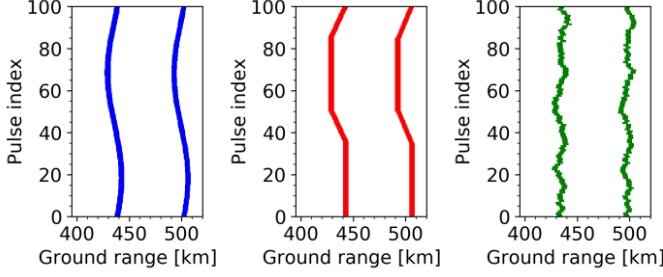


Fig. 6. Swath decrease at a slant range around $R_0 = 700$ km as a result of the sinusoidal PRI variation in (11) with $N = 100$ and $A = 0.007$ (left), the square wave PRI variation of (12) with $N = 100$ and $A = 0.007$ (center) and a random PRI variation of (13) with $N = 100$ and $A = 0.007\sqrt{n_t} = 0.028$ (right). The swath reduction is in all cases less than 14 km.

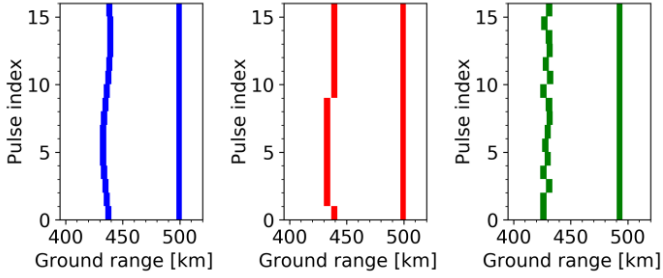


Fig. 7. Swath decrease for the case $N = n_t = 16$ at a slant range around $R_0 = 700$ km as a result of the sinusoidal PRI variation in (11) (left), the square wave PRI variation of (12) (center) and a random PRI variation of (13), all with $A = 0.05$. The swath reduction is in all cases less than 4 km.

C. Decorrelation and Along-Track Baseline

The PRI variation scheme and its parameters N and A have to be selected for a given along-track baseline in order to provide a substantial decorrelation of azimuth ambiguities, while keeping the swath reduction as small as possible.

The trend of ambiguity decorrelation versus along-track baseline can be obtained for a specific set of system parameters and an along-track baseline by means of simulation. For a periodic PRI sequence, this trend will also be periodic with period $B_{a_{period}}$ given by

$$B_{a_{period}} = 2 v_g \sum_{k=0}^{N-1} PRI_k \cong 2 v_g N PRI_{mean} \quad (17)$$

This means that for an along-track baseline equal to integer multiples of $B_{a_{period}}$ the samples of master and slave in spite of the PRI variation and the non-zero along-track baseline will still be available at the same positions and will not determine any ambiguity decorrelation.

Given a sequence of PRI and an along-track baseline, it is possible to assess the resulting ambiguity decorrelation by convolving the impulse response of the ambiguity, which is in general different for the master and slave images, with fully-developed speckle and estimating the coherence. For sinusoidal and square wave PRI variations, it can be observed that the coherence of the ambiguities decreases as the along-track baseline increases from 0 to $B_{a_{period}}/2$ (or from $p B_{a_{period}}$ to

$p B_{a_{period}} + B_{a_{period}}/2$, with $p \in \mathbb{N}$), as the relative shift between the available samples of master and slave increases. Likewise, as the along-track baseline increases from $B_{a_{period}}/2$ to $B_{a_{period}}$ (or from $p B_{a_{period}} + B_{a_{period}}/2$ to $(p+1)B_{a_{period}}$, with $p \in \mathbb{N}$), the coherence of the ambiguities increases. The maximum decorrelation therefore occurs for

$$B_a = (p + 1/2)B_{a_{period}}, p \in \mathbb{N} \quad (18)$$

where \mathbb{N} also includes 0. For random PRI variations the along-track baseline that leads to the maximum ambiguity decorrelation depends on the specific PRI realizations, still the minimum usually corresponds to the value of B_a given in (18).

These considerations therefore suggest that the length N of the PRI sequence can be selected (at least for sinusoidal and square wave schemes) so that the maximum decorrelation is obtained. By substituting (17) in (18) it holds

$$N \cong \frac{B_a}{2(p+1/2)v_g PRI_{mean}}, p \in \mathbb{N} \quad (19)$$

The expression in (19) provides a set of possible values of N , which can be obtained by varying the integer variable p and, if needed, to some extent the value of PRI_{mean} , assuming that B_a and v_g are given. For $B_a = 290$ m, $v_g = 7040$ m/s and $PRI_{mean} = 0.303$ ms, for instance, we can choose $N = 136$ (corresponding to $p = 0$ and belonging to the case $N \gg n_t$), but also $N = 16$ (corresponding to $p = 4$ and belonging to the case $N = n_t$) or other further values of N .

Once different options for the sequence length are available, the parameter A , related to the PRI span, needs to be selected. In general, the higher the PRI span, the more substantial the ambiguity decorrelation, but also the more significant the swath reduction.

2-D simulations have been carried out for a typical spaceborne scenario and the same sequences for which the swath reduction had been assessed in Figs. 6 and 7. The coherence has been estimated using a 9×9 -pixel window. Fig. 8 shows for the aforementioned PRI variations the coherence of the ambiguities as a function of the along-track baseline. These plots have to be considered as periodical, i.e., they repeat with a period given by the maximum along-track baseline given in the plot.

It can be noticed that long sequences allow decorrelation for larger along-track baselines, although one could also exploit in some cases the periodical effect with short sequences. As is apparent, for comparable swath reduction, the square wave PRI variation allows in both cases for the highest decorrelation, while a random PRI variation is less effective, especially if the length of the sequence of PRIs is equal to the number of traveling pulses. From Fig. 8 (b) it can also be noticed that in this example, which refers to the TanDEM-X system, substantial ambiguity decorrelation can be achieved, as long as the along-track baseline is larger than 20 m.

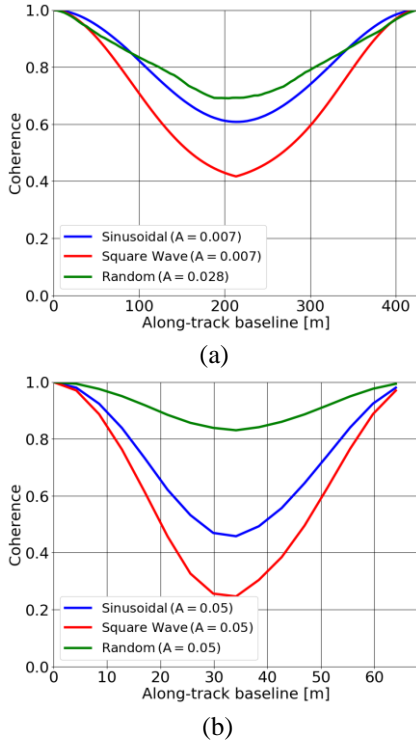


Fig. 8. Coherence of the ambiguities as a function of the along-track baseline for the sinusoidal PRI variation in (11) (blue), the square wave PRI variation of (12) (red) and the random PRI variation of (13) (green). (a) $N = 100$ (length of the sequence of PRIs is much larger than the number of traveling pulses), corresponding to swath width reduction depicted in Fig. 6. (b) $N = 16$ sinusoidal PRI variation (length of the sequence of PRIs equal to the number of traveling pulses), corresponding to swath width reduction depicted in Fig. 7.

It is worth to notice that the minimum and maximum PRIs of the square wave variations of Figs. 6 and 7 correspond to differences of the instantaneous PRFs in the order of 55 Hz and 330 Hz, respectively. This means that in order to achieve a significant decorrelation of azimuth ambiguities in the single-pass case an instantaneous PRF change much larger than the PRF difference required for the repeat-pass case (only 8 Hz in the example of Section II) is needed.

At the end of Section II, it was observed that the PRF difference also determines a relative shift of range ambiguities. In the single-pass case, as a consequence of the continuous PRI variation range ambiguous echoes appear at different ranges for each pulse, i.e., they spread over several range resolution cells, and are also likely to be decorrelated [29].

IV. IMPACT ON INTERFEROGRAM AND DEM QUALITY

In order to assess the impact of ambiguity decorrelation on interferogram and DEM quality, simulations are performed starting from the dataset of Fig. 1.

After having removed azimuth ambiguities from both the master and slave images using a Wiener filter (which provides an ambiguity suppression relative to the main signal suppression of about 11 dB), ambiguities have been artificially reintroduced in both the master and slave images by convolving the focused image with the IRF of the focused first-order azimuth ambiguity, translating it, and scaling it according to the desired ambiguity-to-signal ratio. Furthermore, the ambiguity decorrelation has been introduced by multiplying the

interferogram of the ambiguities by a phase screen generated according to the statistical distribution corresponding to the desired decorrelation level [1].

Figs. 9 and 10 show the resulting interferometric phase, the magnitude of the complex coherence, and the DEM obtained after phase unwrapping, for systems with $AASR = -17$ dB and $AASR = -22$ dB, respectively. Both the case of no decorrelation and that of a coherence of the interferogram of ambiguities equal to 0.3, i.e., corresponding to almost complete ambiguity decorrelation, have been considered.

Fig. 9 corresponds to an $AASR = -17$ dB and shows that in the absence of ambiguity decorrelation strong circular artifacts appear in both the interferometric phase and in the DEM. The same artifacts appear as a slight noise-like disturbance for the same $AASR$ level and decorrelated ambiguities. The visual comparison of Figs. 9 (bottom) and 10 (top) also shows that the disturbance pattern obtained for $AASR = -17$ dB and decorrelated ambiguities is very similar to that obtained for $AASR = -22$ dB and coherent ambiguities, which confirms that decorrelating azimuth ambiguities through slight PRI variation represents a viable alternative to support demanding $AASR$ requirements.

Whereas coherent effects of azimuth ambiguities are more apparent in low backscatter areas such as water or sea ice, phase bias can also be noticeable and lead to nonnegligible height biases over land scenes. Fig. 11 shows a further simulation using a TanDEM-X data set acquired near Klagenfurt am Wörthersee, Austria, and assuming $AASR = -17$ dB. The portions of the SAR image responsible for and affected by azimuth ambiguities are shown in Fig. 11 (a) and (b), respectively. The phase bias in the area affected by ambiguities in the case of no decorrelation and that of an ambiguity decorrelation equal to 0.3, i.e., corresponding to almost complete ambiguity decorrelation, is displayed in Fig. 11 (c) and (d), respectively. In this example the ambiguity decorrelation leads to a decrease of the average absolute phase bias from 7.1° to 4.6° , corresponding to a decrease of the average absolute height bias from 91 to 58 cm.

V. CONCLUSION AND OUTLOOK

This paper tackles the problem of artifacts appearing in SAR interferograms as a result of the coherent interference of azimuth ambiguities and proposes a solution based on ambiguity decorrelation, which can be used as an alternative to or even in combination with other postprocessing techniques.

For the repeat-pass case, it is shown that it is enough to use two slightly different PRFs for the two acquisitions to decorrelate azimuth ambiguities. An analytical expression is provided for the minimum required PRF difference, which amounts to only few Hz for TanDEM-X. It is also mentioned that this PRF difference additionally shifts range ambiguities and therefore prevents possible coherence interference effects.

For the single-pass case, a slight variation of the PRI during the acquisition helps decorrelating ambiguities, if an along-track baseline is present. For TanDEM-X, an along-track baseline larger than 20 m is required to achieve substantial ambiguity decorrelation. In particular, it is shown that the square wave PRI variation, i.e., repeating $N/2$ times a given PRI, then $N/2$ times a second PRI, then again $N/2$ times the first

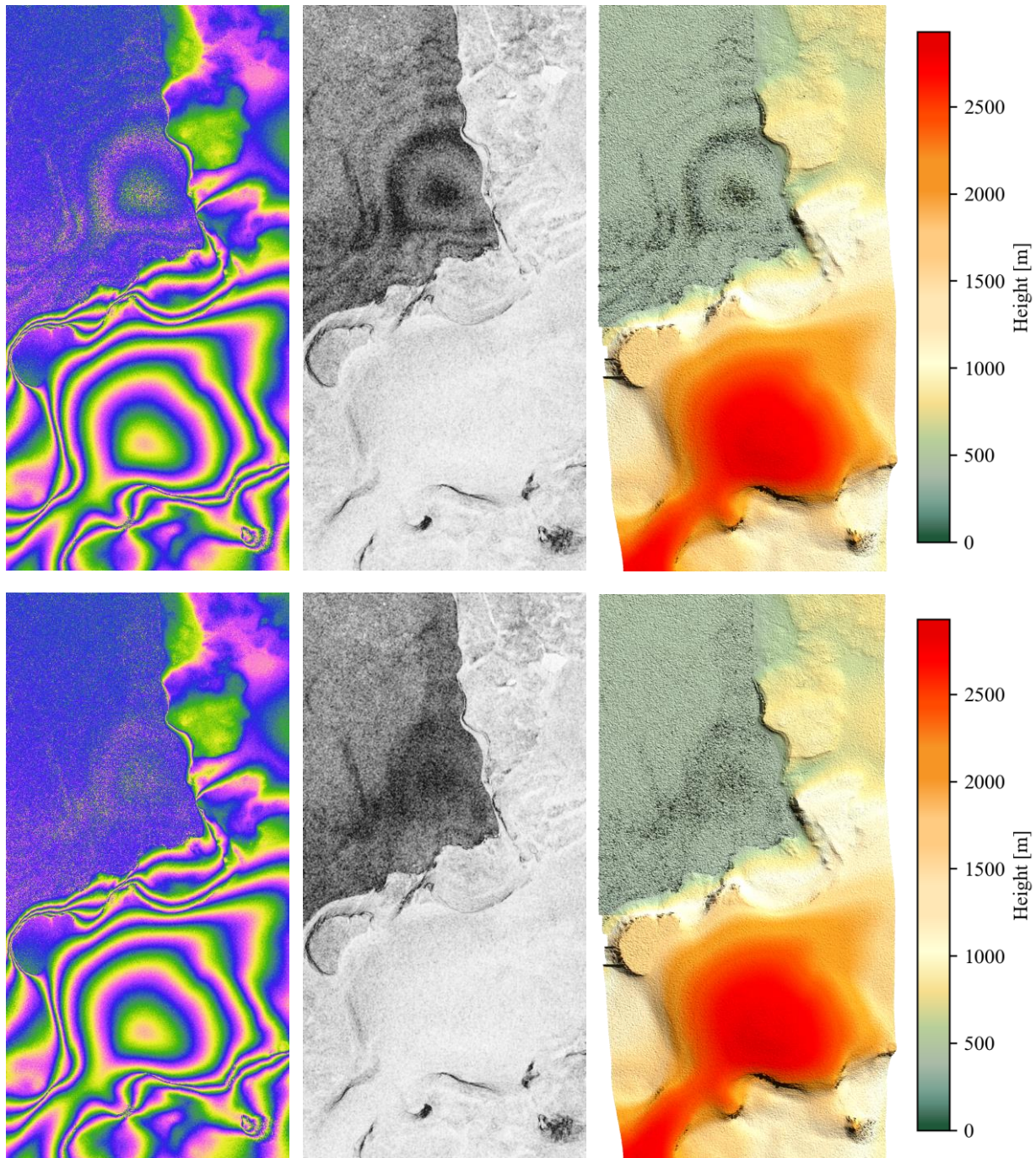


Fig. 9. Impact of ambiguity decorrelation on interferometric phase (left), magnitude of the complex coherence (center), and DEM (right) for AASR = -17 dB. (top) No decorrelation. (bottom) Coherence of the ambiguity = 0.3. The horizontal and vertical axes represent ground range (5.12 km) and azimuth (10.24 km), respectively.

PRI and so on, performs best. The square wave PRI variation is also the easiest to implement in most systems, e.g., it is the only one that can be straightforwardly implemented in TanDEM-X, as it does not require an extremely fine PRI variation. The PRI variation scheme needs to account for the along-track baseline of the acquisition and to be optimized accordingly. It could be investigated whether waveform diversity in addition to PRI variation could help achieving further ambiguity decorrelation.

While an accurate performance assessment can only be made

for a specific system, simple simulations under conservative assumptions show the effectiveness of the technique, which could be useful for the design of future spaceborne interferometric SAR systems, such as High Resolution Wide Swath (HRWS) [36], as well as for the enhanced exploitation of current ones.

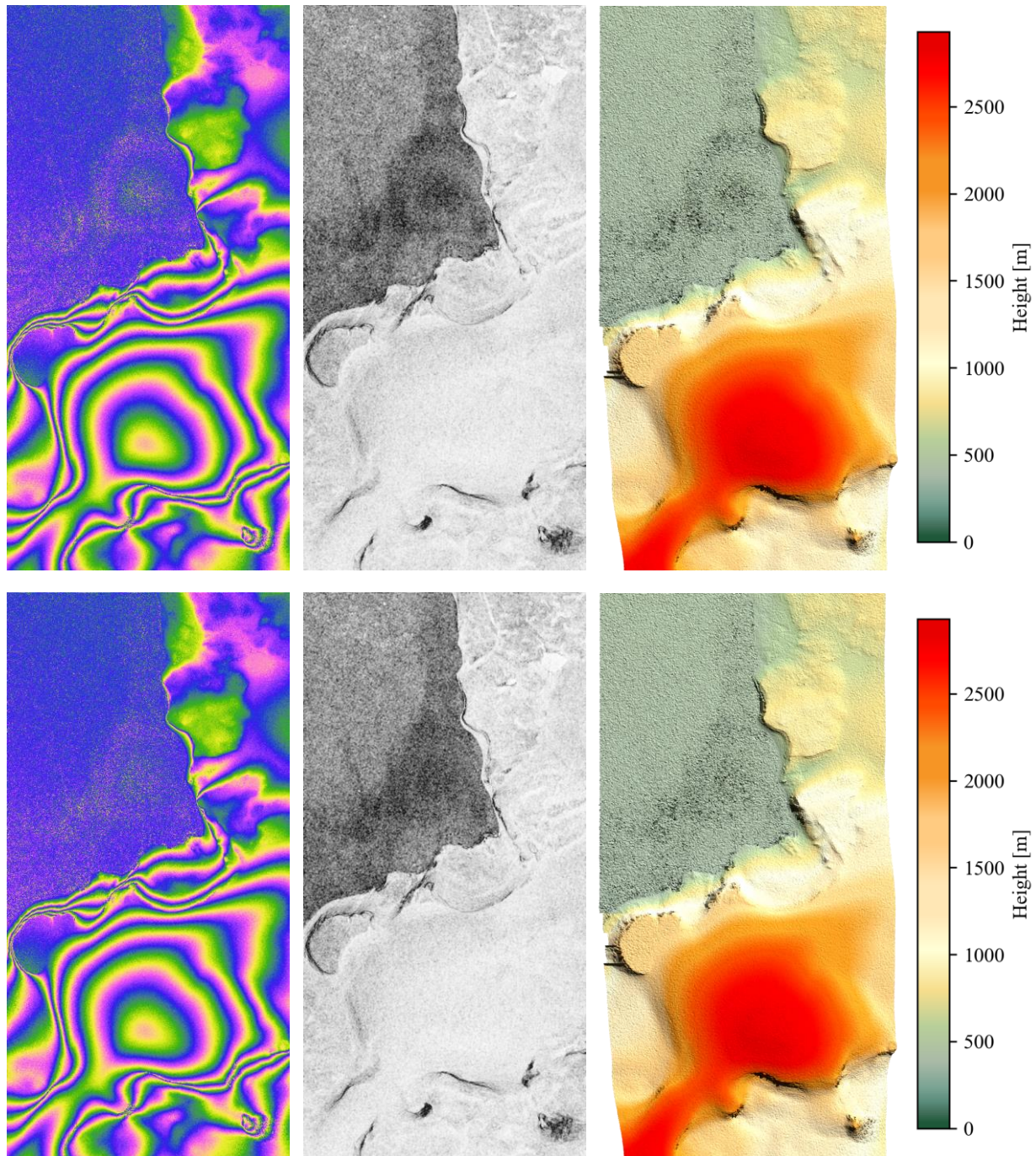


Fig. 10. Impact of ambiguity decorrelation on interferometric phase (left), magnitude of the complex coherence (center), and DEM (right) for AASR = -22 dB. (top) No decorrelation. (bottom) Coherence of the ambiguity = 0.3. The horizontal and vertical axes represent ground range (5.12 km) and azimuth (10.24 km), respectively.

REFERENCES

- [1] R. Bamler and P. Hartl, "Synthetic aperture radar interferometry," *Inv. Probl.*, vol. 14, no. 4, pp. R1–R54, Feb. 1998.
- [2] P. A. Rosen *et al.*, "Synthetic aperture radar interferometry," *Proc. IEEE*, vol. 88, no. 3, pp. 333–382, March 2000.
- [3] R. F. Hanssen, *Radar interferometry: data interpretation and error analysis*, Springer, Dordrecht, The Netherlands, 2001.
- [4] A. Moreira, P. Prats-Iraola, M. Younis, G. Krieger, I. Hajnsek and K. P. Papathanassiou, "A tutorial on synthetic aperture radar," *IEEE Geosci. Rem. Sens. Mag.*, vol. 1, no. 1, pp. 6–43, March 2013.
- [5] H. A. Zebker and J. Villasenor, "Decorrelation in interferometric radar echoes," *IEEE Trans. Geosci. Rem. Sens.*, vol. 30, no. 5, pp. 950–959, Sept. 1992.
- [6] G. Krieger, A. Moreira, H. Fiedler, I. Hajnsek, M. Werner, M. Younis, and M. Zink, "TanDEM-X: A satellite formation for high-resolution SAR interferometry," *IEEE Trans. Geosci. Remote Sens.*, vol. 45, no. 11, pp. 3317–3341, Nov. 2007.

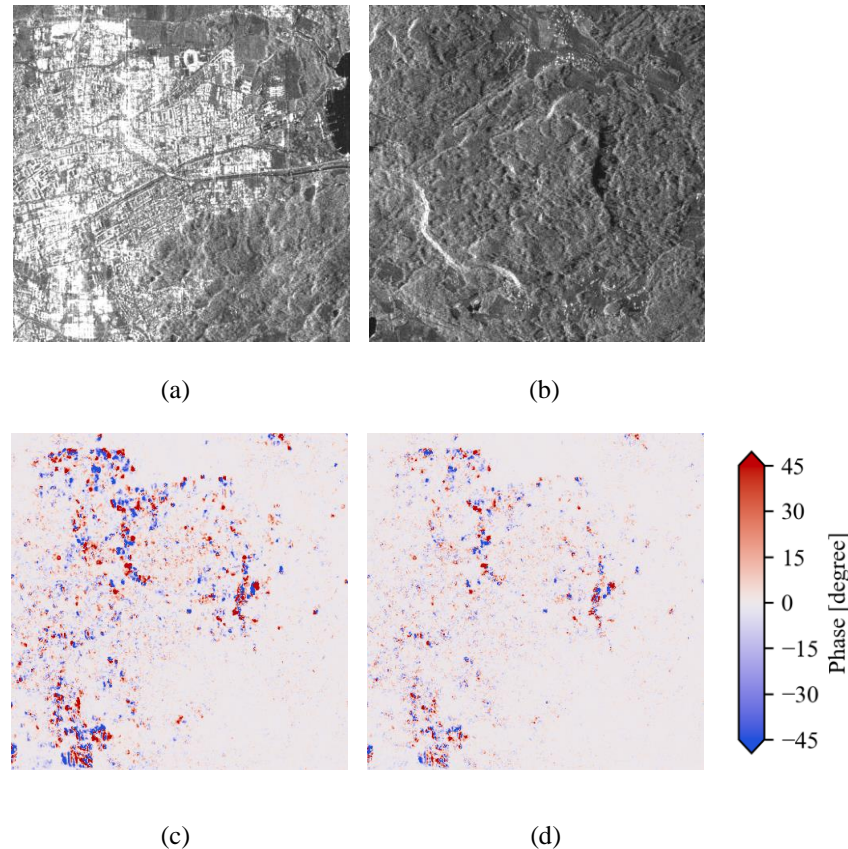


Fig. 11. Example of impact of ambiguity decorrelation on a land scene using a TanDEM-X data set acquired near Klagenfurt am Wörthersee. (a) Portion of the SAR image (amplitude) responsible for azimuth ambiguities. (b) Portion of the SAR image (amplitude) affected by azimuth ambiguities. (c) Phase bias in the area affected by ambiguities in the case of no decorrelation. (d) Phase bias in the area affected by ambiguities in the case of ambiguity decorrelation equal to 0.3. The horizontal and vertical axes represent ground range (4.93 km) and azimuth (4.11 km), respectively.

- [7] D. Massonnet, "Capabilities and limitations of the interferometric cartwheel," *IEEE Trans. Geosci. Remote Sens.*, vol. 39, no. 3, pp. 506-520, March 2001.
- [8] R. Fjortoft, J.-C. Souyris, J.-M. Gaudin, P. Durand, and D. Massonnet, "Impact of ambiguities in multistatic SAR: some specificities of an L-band interferometric cartwheel," *IGARSS 2004. 2004 IEEE International Geoscience and Remote Sensing Symposium*, 2004, pp. 1754-1757, vol. 3.
- [9] M. Villano and G. Krieger, "Impact of Azimuth Ambiguities on Interferometric Performance," *IEEE Geosci. Rem. Sens. Lett.*, vol. 9, no. 5, pp. 896-900, Sept. 2012.
- [10] M. Villano and G. Krieger, "Spectral-Based Estimation of the Local Azimuth Ambiguity-to-Signal Ratio in SAR Images," *IEEE Trans. Geosci. Remote Sens.*, vol. 52, no. 5, pp. 2304-2313, May 2014.
- [11] M. Villano and G. Krieger, "Accounting for azimuth ambiguities in interferometric performance analysis," *2012 IEEE Int. Geosci. Rem. Sens. Symposium*, 2012, pp. 299-302.
- [12] A. Moreira, "Suppressing the azimuth ambiguities in synthetic aperture radar images," *IEEE Trans. Geosci. Remote Sens.*, vol. 31, no. 4, pp. 885-895, July 1993.
- [13] A. Monti Guarnieri, "Adaptive removal of azimuth ambiguities in SAR images," *IEEE Trans. Geosci. Remote Sens.*, vol. 43, no. 3, pp. 625-633, Mar. 2005.
- [14] Z. Yu and M. Liu, "Suppressing azimuth ambiguity in spaceborne SAR images based on compressed sensing," *Science China Information Sciences*, vol. 55, no. 8, pp. 1830-1837, 2012.
- [15] M. Liu, Z. Yu, and C. Li, "Azimuth ambiguity suppression for spaceborne SAR based on PRF micro-variation," *2013 IEEE Int. Geosci. and Rem. Sens. Symposium*, 2013.
- [16] J. Chen, M. Iqbal, W. Yang, P. Wang, and B. Sun, "Mitigation of azimuth ambiguities in spaceborne stripmap SAR images using selective restoration," *IEEE Trans. Geosci. Remote Sens.*, vol. 52, no. 7, pp. 4038-4045, Jul. 2014.
- [17] G. Di Martino, A. Iodice, D. Riccio, and G. Ruello, "Filtering of azimuth ambiguity in stripmap synthetic aperture radar images," *IEEE J. Sel. Top. Appl. Earth Obs. Rem. Sens.*, vol. 7, no. 9, pp. 3967-3978, 2014.
- [18] J. Chen, K. Wang, W. Yang, and W. Liu, "Accurate reconstruction and suppression for azimuth ambiguities in spaceborne stripmap SAR images," *IEEE Geosci. Rem. Sens. Lett.*, vol. 14, no. 1, pp. 102-106, 2016.
- [19] Y. Long, F. Zhao, M. Zheng, G. Jin, and H. Zhang, "An azimuth ambiguity suppression method based on local azimuth ambiguity-to-signal ratio estimation," *IEEE Geosci. Rem. Sens. Lett.*, vol. 17, no. 12, pp. 2075-2079, 2020.
- [20] P. López-Dekker, Y. Li, L. Iannini, P. Prats-Iraola and M. Rodríguez-Cassola, "On Azimuth Ambiguities Suppression for Short-Baseline Along-Track Interferometry: the Stereoid Case," *2019 IEEE Int. Geosci. Rem. Sens. Symposium*, 2019, pp. 110-113.
- [21] D. Richter, M. Rodríguez Cassola, M. Zonno, and P. Prats, "Coherent Azimuth Ambiguity Suppression Based on Linear Optimum Filtering of Short Along-Track Baseline SAR Interferograms," *European Conference on Synthetic Aperture Radar (EUSAR)*, Leipzig, Germany, 25-27 July 2022.
- [22] F. K. Li and W. T. K. Johnson, "Ambiguities in spaceborne synthetic aperture radar systems," *IEEE Trans. Aerosp. Electron. Syst.*, vol. 19, no. 3, pp. 389-397, May 1983.
- [23] R. K. Raney and G. J. Princz, "Reconsideration of Azimuth Ambiguities in SAR," *IEEE Trans. Geosci. Remote Sens.*, vol. GE-25, no. 6, pp. 783-787, Nov. 1987.

- [24] N. Ustalli and M. Villano, "Impact of Ambiguity Statistics on Information Retrieval for Conventional and Novel SAR Modes," *2020 IEEE Radar Conf.*, 2020, pp. 1-6.
- [25] M. Villano, G. Krieger and A. Moreira, "Nadir Echo Removal in Synthetic Aperture Radar via Waveform Diversity and Dual-Focus Postprocessing," *IEEE Geosci. Rem. Sens. Lett.*, vol. 15, no. 5, pp. 719-723, May 2018.
- [26] S. -Y. Jeon, T. Kraus, U. Steinbrecher, G. Krieger and M. Villano, "Experimental Demonstration of Nadir Echo Removal in SAR Using Waveform Diversity and Dual-Focus Postprocessing," *IEEE Geosci. Rem. Sens. Lett.*, vol. 19, pp. 1-5, 2022, Art no. 4015605, doi: 10.1109/LGRS.2021.3095566.
- [27] M. Villano, G. Krieger, and A. Moreira, "Staggered SAR: High-Resolution Wide-Swath Imaging by Continuous PRI Variation," *IEEE Trans. Geosci. Remote Sens.*, vol. 52, no. 7, pp. 4462-4479, July 2014.
- [28] M. Villano, G. Krieger, and A. Moreira, "A Novel Processing Strategy for Staggered SAR," *IEEE Geosci. Rem. Sens. Lett.*, vol. 11, no. 11, pp. 1891-1895, November 2014.
- [29] M. Villano, "Staggered Synthetic Aperture Radar," PhD Thesis, Karlsruhe Institute of Technology, DLR-Forschungsbericht 2016-16, ISSN 1434-8454, Wessling, Germany, 2016.
- [30] M. Villano, G. Krieger, M. Jäger, and A. Moreira, "Staggered SAR: Performance Analysis and Experiments with Real Data," *IEEE Trans. Geosci. Remote Sens.*, vol. 55, no. 11, pp. 6617-6638, Nov. 2017.
- [31] M. Villano and M. N. Peixoto, "Characterization of Nadir Echoes in Multiple-Elevation-Beam SAR with Constant and Variable Pulse Repetition Interval," *IEEE Trans. Geosci. Remote Sens.*, vol. 60, 2022.
- [32] M. Villano, M. Nogueira Peixoto, N. Ustalli, G. Krieger, A. Moreira, "Staggered SAR: Recent Advances and Design Trade-Offs," European Conference on Synthetic Aperture Radar (EUSAR), Leipzig, Germany, 29 March -1 April 2021.
- [33] M. Pinheiro, P. Prats-Iraola, M. Rodriguez-Cassola, M. Villano, "Analysis of low-oversampled staggered SAR data", *IEEE J. Sel. Top. Appl. Earth Obs. Rem. Sens.*, vol. 13, 2020.
- [34] M. Pinheiro *et al.*, "Processing and Performance Analysis of NASA-ISRO SAR (NISAR) Staggered Data," *IGARSS 2019 - 2019 IEEE International Geoscience and Remote Sensing Symposium*, 2019, pp. 8374-8377.
- [35] H. A. Zebker, "A Signal Model for PRF Dithering in Wide-Swath, Fine-Resolution InSAR," *IEEE Geosci. Rem. Sens. Lett.*, vol. 18, no. 7, pp. 1214-1218, July 2021.
- [36] J. Mittermayer, G. Krieger, A. Bojarski, M. Zonno, M. Villano, M. Pinheiro, M. Bachmann, S. Buckreuss, and A. Moreira, "MirrorSAR: An HRWS Add-On for Single-Pass Multi-Baseline SAR Interferometry," *IEEE Trans. Geosci. Remote Sens.*, vol. 60, 2022.